Hollow Microspherical Li[Li$_{0.24}$Ni$_{0.38}$Mn$_{0.38}$]O$_2$ as Cathode Material for Lithium-Ion Batteries with Excellent Electrochemical Performance

Shumei Dou[*], Ping Li, Huiqin Li[*]

Engineering research center of advanced ferroelectric functional materials, Shaanxi Key Laboratory of Phytochemistry, College of Chemistry and Chemical Engineer, Baoji University of Arts and Sciences, Baoji, Shaanxi, China 721013
[*]E-mail: dsmwxsh@163.com; snowtrue@126.com

Li-rich hollow microspherical Li[Li$_{0.24}$Ni$_{0.38}$Mn$_{0.38}$]O$_2$ sample was successfully synthesized by a coprecipitation approach followed by high-temperature calcinations. The compositions and structures of Li-rich hollow microspherical Li[Li$_{0.24}$Ni$_{0.38}$Mn$_{0.38}$]O$_2$ were investigated by X-ray diffraction (XRD), scanning electron microscopy (SEM), and X-ray photoelectron spectroscopy (XPS) and the results revealed that the sample possesses typical a-NaFeO$_2$ layered structures with a weak reflection of LiMnO$_6$, and of hollow microspherical morphology with porous surfaces. Electrochemical measurements showed that the Li-rich hollow microspheres deliver good cycling stabilities and rate capabilities with initial discharge capacities of 229, 213 and 202 mAh g^{-1} at current density of 340, 680 and 1000 mA g^{-1}, respectively, with fewer capacity above 4.5 V than that of Li-rich spinel-layered Li–Ni–Mn–Co–O cathode materials. The excellent electrochemical performances of hollow microspherical Li-rich Li[Li$_{0.24}$Ni$_{0.38}$Mn$_{0.38}$]O$_2$ could be related to the synergistic effect of well-regulated morphologies and appropriate sizes as well as the porous surfaces.

1. INTRODUCTION

Rechargeable Li-ion batteries have been widely utilized in various instruments that uses electrisity such as in tablet computers, mobile phones and other portable electronic devices as well as in the field of energy-storage power stations, electric vehicles, medical equipments, aerospaces. Such batteries have the potential for broad application in the future because they meet most of performance requirements, such as high energy and high power density. The demands for the next generation Li-ion

batteries with high-performances have increased in terms of improved energy density, safety and cost [1]. Among all the available options, adopting cathodes with higher capacities are one of the most effective approaches to improve the energy density [2, 3]. On this point, composites of Li_2MnO_3 and $LiNi_{0.5}Mn_{0.5}O_2$ have many advantages, such as delivering high discharge capacities of more than 250 mAh g^{-1} in the voltage range of 2.0-4.8 V and exhibiting excellent cycling performances [4-6], which make them ideal candidates as cathode materials.

However, these Li-rich materials suffer from some drawbacks, including large irreversible capacity losses in the initial cycle, capacity and discharge voltage fading in subsequent cycles and so on [7, 8]. Considerable efforts have been applied to improve the electrochemical properties of cathode materials by doping with ions [9-14] to stabilize the crystal structure, applying surface coatings [15-20] to suppress undesired surface side reactions, utilizing different morphologies or particle sizes [21-28] to reduce the Li-ion diffusion length, and so on. However, during the 1st charging process, irreversible oxygen loss also occurs, leading to a large irreversible capacity and subsequent deterioration of the cycling performance [29].

The effective way to improve the rate performances of the cathode materials is to reduce the particle size to nanoscale levels owing to shortened Li-ion diffusion pathways. However, side reactions can be promoted due to the low tap density and high surface area of nanoscale particles. In contrast, microsized spherical particles have some advantagies such as better fluidity, and dispersity than irregular particles, as well as higher tap densities[30], which are suitable for preparing cathode materials. Therefore, Li-rich materials with porous microstructures are highly desired for Li-ion batteries.

In our work, Li-rich hollow microspherical $Li[Li_{0.24}Ni_{0.38}Mn_{0.38}]O_2$ was successfully synthesized by a coprecipitation approach followed by high-temperature calcination. Further, the structure and electrochemical properties of this material were investigated.

2. EXPERIMENT

2.1 Synthesis of Li[Li$_{0.24}$Ni$_{0.38}$Mn$_{0.38}$]O$_2$

$Li[Li_{0.24}Ni_{0.38}Mn_{0.38}]O_2$ materials were prepared by a solid state reaction from lithium carbonate (Li_2CO_3) and nickel-manganese carbonate ($Ni_{0.5}Mn_{0.5}CO_3$) [31]. Nickel-manganese carbonate was prepared by coprecipitation from aqueous mixture of $NiSO_4 \cdot 6H_2O$, $MnSO_4 \cdot H_2O$ (Ni:Mn = 1:1, molar ratio; the combined concentration was 0.04 mol L^{-1}, marked solution A) and 0.10 mol L^{-1} Na_2CO_3 aqueous solution (marked solution B). The solution A and B were mixed slowly in a reactor filled with nitrogen with continuous stirring. The pH of the mixed solution was kept in the range of 8~9 at 55 °C during the precipitation process. As-synthesized precursor $Ni_{0.5}Mn_{0.5}CO_3$ was collected by suction filtracion and wash them quickly and then dry at around 100 °C under vacuum about 10 h. To prepare $Li[Li_{0.24}Ni_{0.38}Mn_{0.38}]O_2$, the obtained $(Mn_{0.5}Ni_{0.5})CO_3$ and Li_2CO_3 were mixed at a molar ratio of 1:0.78 by grinding with absolute ethyl alcohol, and the mixture was pressed into pellets. The pellets were heated at 500 °C for 3 h in air before heating up to 900 °C for 15 h and then

quenched to room temperature.

2.2. Materials characterization

XRD patterns of the samples were investigated with a D/MAX-2500 X-ray diffractometer (made in Japan) using Cu Kα radiation in the 2 theta range of 10-80°. The contents of the elements in the synthesized samples were determined by inductively coupled plasma (ICP) that recorded on Thermo Fisher ICAP 6300. The morphology and particle size of the samples were investigated by field emission scanning electron microscopy (SEM) on a JSM-6700F instrument working at 5 KV. The valence states of metal ions were determined by X-ray photoelectron spectroscopy (XPS) performed on an ESCA-LAB MKⅡ apparatus performed with a monochromatic Al Kα X-ray source.

2.3. Electrochemical measurements

Charge and discharge profiles were collected by galvanostatically cycling between 2.5 and 4.8 V (Shenzhen Neware, BTS, China). For the preparation of cathode sheets, slurry was formed by mixing the active material, acetylene black, and binder (polyvinylidene fluoride, dissolved in N-methyl-2-pyrrolidone) in a weight ratio of 8:1:1. The slurry was spread uniformly on aluminium foil substrate, cut into slices (1cm×1cm) as the electodes and yielding an active material loading of 0.4 mg cm^{-1}. The electrodes were dried under vacuum at 120 °C for 10 h and then pressed under 60 MPa and weighted. 1 M $LiPF_6$ in a 1:1 ethylene carbonate/diethyl carbonate was used as electrolyte, and lithium foil was used as anode. A thin sheet of microporous polypropylene insulated the positive electrode from negative electrodes. Battery assembly was carried out in an argon-filled glove box. Cyclic voltammetry (CV) were carried out on electrochemical workstation (CHI 660C) with a scan range of 2.5-4.8 V (vs.Li/Li$^+$) at a scan rate of 0.2 mV s^{-1}.

3. RESULTS AND DISCUSSION

The chemical compositions (wt.%) of the prepared precursor and product determined by ICP are summarized in Table 1. The measured cation ratios of Ni:Mn and Li:Ni:Mn are in good agreement with the intended composition, which implies that the metal oxides react homogeneously.

Table 1. Chemical composition (wt. %) of the prepared precursor and product determined by ICP.

Li	Ni	Mn	Formula
-	25.74	24.48	$Ni_{0.49}Mn_{0.50}CO_3$
9.87	28.62	25.16	$Li_{1.18}Ni_{0.40}Mn_{0.38}O_2$

The XRD pattern of spherical $Ni_{0.5}Mn_{0.5}CO_3$ precursor is shown in Figure 1. All the diffraction peaks of $Ni_{0.5}Mn_{0.5}CO_3$ can be readily indexed to a hexagonal structure belonging to space group R-3c, which is consistent with isostructural $MnCO_3$, where some Mn has been replaced by Ni within the carbonate matrix.

The XRD patterns of the Li-rich hollow microspherical and nonspherical $Li[Li_{0.24}Ni_{0.38}Mn_{0.38}]O_2$ cathode materials are shown in Figure 2a and 2b.

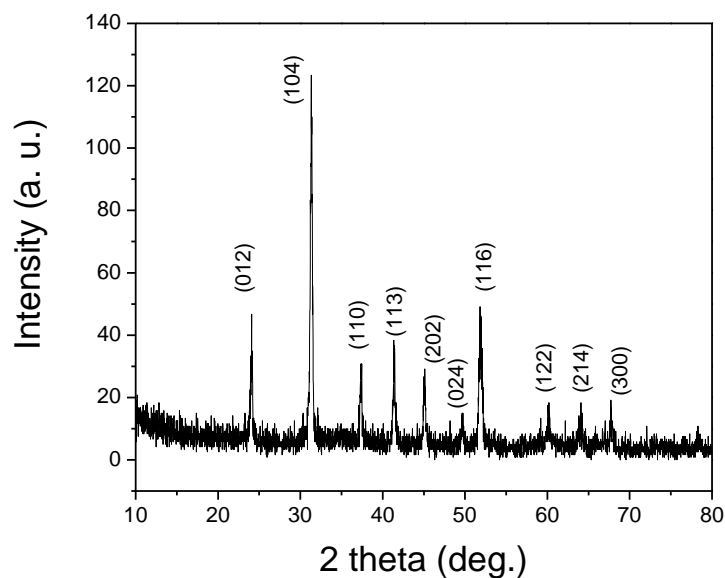**Figure 1.** XRD pattern of spherical $(Ni_{0.5}Mn_{0.5})CO_3$ precursor.

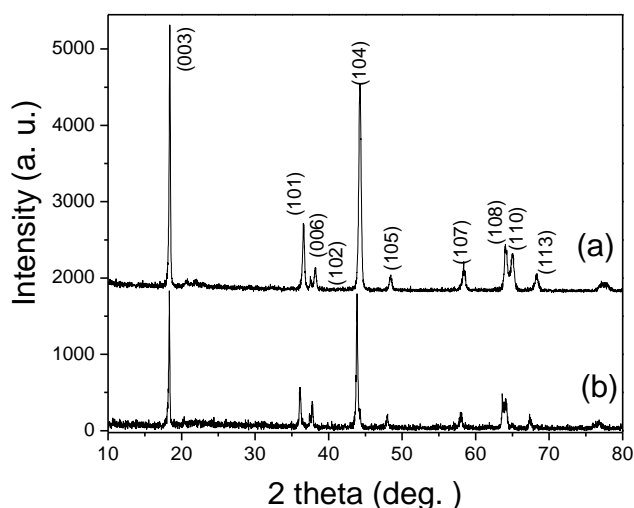**Figure 2.** XRD patterns of hollow spherical (a) and nonspherical (b) $Li[Li_{0.24}Ni_{0.38}Mn_{0.38}]O_2$.

Both samples exhibit the characteristic patterns of a-$NaFeO_2$ with a layered hexagonal structure. All peaks can be indexed to a layered structure belonging to the space group R-3m (No. 166), except the peaks between 20° and 25°. The weak reflections in this region can be indexed to the

monoclinic C2/m space group, corresponding to $LiMnO_6$ cation ordering in the transition metal layers of Li_2MnO_3 [32-34]. The clear separation of adjacent (006)/(012) and (108)/(110) peaks for hollow spherical $Li[Li_{0.24}Ni_{0.38}Mn_{0.38}]O_2$ (Figure 2a) indicates that the hollow spheres have a more crystalline layered structure than nonspherical $Li[Li_{0.24}Ni_{0.38}Mn_{0.38}]O_2$.
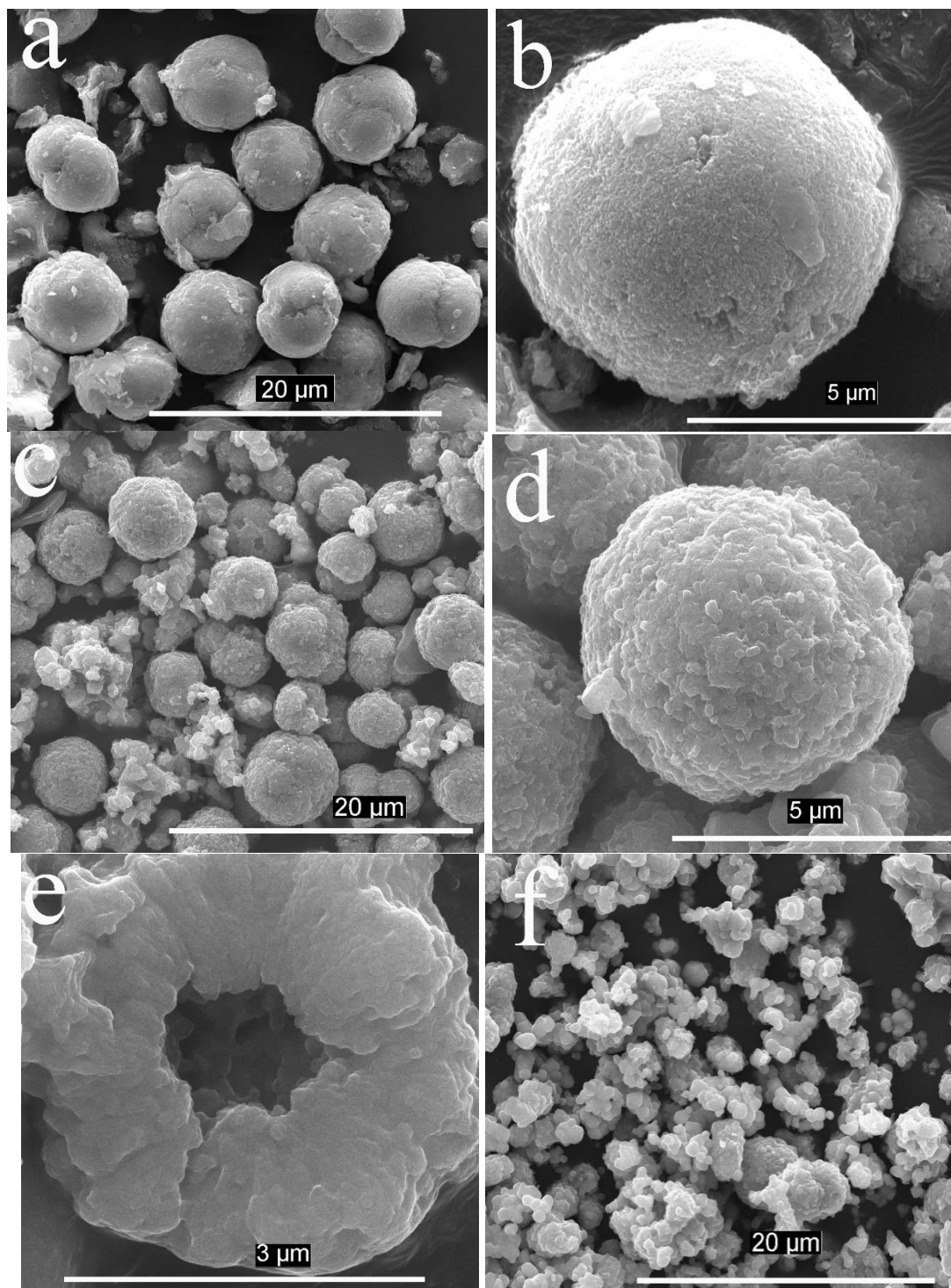

Figure 3. SEM images of spherical precursor (a) and (b), hollow microspherical $Li[Li_{0.24}Ni_{0.38}Mn_{0.38}]O_2$ (c), (d) and (e), nonspherical $Li[Li_{0.24}Ni_{0.38}Mn_{0.38}]O_2$ (f).

Figure 3 shows typical SEM images of the spherical precursor, and hollow microspherical and nonspherical $Li[Li_{0.24}Ni_{0.38}Mn_{0.38}]O_2$. It was found that the $(Ni_{0.5}Mn_{0.5})CO_3$ precursor has a spherical morphology consisting of particles of 3–7 mm in diameter with relatively smooth surfaces (figure 3a and 3b). After high temperature calcination with Li_2CO_3, the formed $Li[Li_{0.24}Ni_{0.38}Mn_{0.38}]O_2$ microspheres maintained the spherical morphology and size of the $(Ni_{0.5}Mn_{0.5})CO_3$ precursor (figure 3c). The high-magnification SEM images in Figure 3d reveal that the $Li[Li_{0.24}Ni_{0.38}Mn_{0.38}]O_2$ microspheres are assembled from primary particles with sizes of 100–200 nm, which form porous surface structures. The inner structure of the $Li[Li_{0.24}Ni_{0.38}Mn_{0.38}]O_2$ microspheres can be determined by examining a cross section of the microspheres. Careful observation revealed that the $Li[Li_{0.24}Ni_{0.38}Mn_{0.38}]O_2$ microspheres have a hollow spherical structure with an inner diameter of ca. 1 mm (figure 3e). Incontrast, the nonspherical aggregates of $Li[Li_{0.24}Ni_{0.38}Mn_{0.38}]O_2$ particles, do not have a uniform morphology (figure 3f).
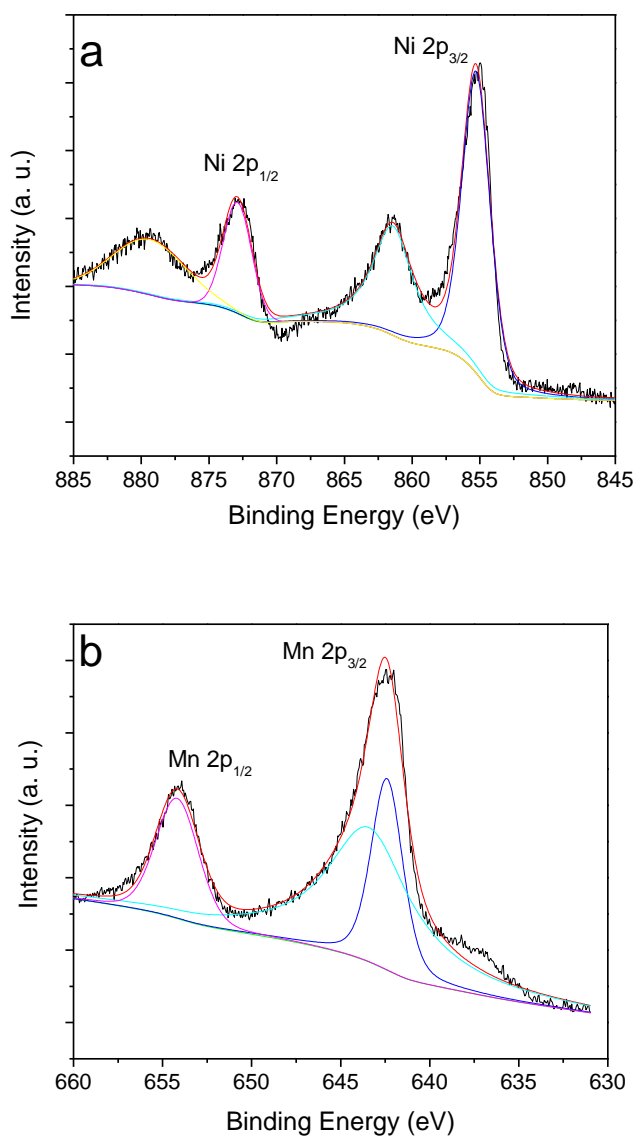

Figure 4. XPS spectra of the hollow microspherical $Li[Li_{0.24}Ni_{0.38}Mn_{0.38}]O_2$ (a) Ni 2p, (b) Mn 2p.

In order to elucidate the valence state of the transition metal in the hollow microspherical $Li[Li_{0.24}Ni_{0.38}Mn_{0.38}]O_2$ materials, XPS spectra were obtained as shown in Figure 4. In the Ni XPS spectrum (Figure 4a), the major Ni 2p peaks have binding energies of 854.8 eV (Ni $2p_{3/2}$) and 872.7 eV (Ni $2p_{1/2}$) with satellite peaks around 861.5 and 879.4 eV. On the one hand, the Ni $2p_{3/2}$ satellite peak is characteristic of Ni^{2+}, identifying with the standard Ni^{2+} in the $LiW_xNi_{0.5}Mn_{1.5-x}O_4$ sample[35]. on the other hand, the binding energy of Ni $2p_{1/2}$ is similar to the Ni^{2+} in the $Li_2MnO_3 \cdot LiMn_{1/3}Ni_{1/3}Co_{1/3}O_2$ [36]. With regarding to the Ni $2p_{3/2}$ main peak, it has been previously reported that the binding energy of Ni^{2+} in $Li_{1.16}Ni_{0.15}Co_{0.19}Mn_{0.50}O_2$ is 854.0 eV [37] and that of Ni^{3+} in $LiNiO_2$ is at 855.5 eV [38]. As for this work, the binding energy at 854.8 eV is exactly located in the range of 854.0 and 855.3 eV, indicating the oxidation state of Ni ions consists of mixed +2 and +3 [39]. The Mn XPS spectrum shows a characteristic Mn $2p_{3/2}$ peak at a binding energy of 643.5 eV (Figure 4b), which is closer to the value measured for Mn^{4+} in l-MnO_2 (642.4 eV) than that for Mn^{3+} in $Li_2Mn_2O_4$ (641.1 eV) [40]. Therefore, the valence of Mn in $Li[Li_{0.24}Ni_{0.38}Mn_{0.38}]O_2$ is considered to be tetravalent, without any Mn^{3+}.

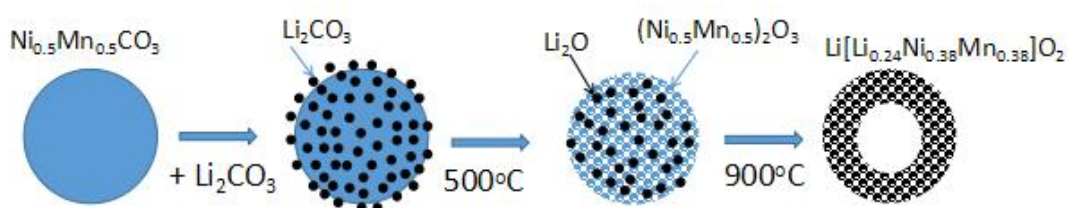**Figure 5.** Schematic illustration of the controlled preparation of hollow microspherical $Li[Li_{0.24}Ni_{0.38}Mn_{0.38}]O_2$.

The fabrication procedure for hollow microspherical $Li[Li_{0.24}Ni_{0.38}Mn_{0.38}]O_2$ can be briefly described in Figure 5. Uniform $Ni_{0.5}Mn_{0.5}CO_3$ microspheres prepared by the precipitation method are employed as the precursor in the synthesis. In the process of grinding the mixture of $Ni_{0.5}Mn_{0.5}CO_3$, Li_2CO_3 and ethanol, Li_2CO_3 is attached to the surface or infiltrated to the inside of the spherical particles in the effects of ethanol. At high temperatures, the mixture of $Ni_{0.5}Mn_{0.5}CO_3$ and Li_2CO_3 undergoes multistep and rather complicated reactions. Firstly, the $Ni_{0.5}Mn_{0.5}CO_3$ microspheres and Li_2CO_3 are converted into $(Ni_{0.5}Mn_{0.5})_2O_3$ and Li_2O by thermal decomposition at 500 °C according to the following chemical equations:

$$2Ni_{0.5}Mn_{0.5}CO_3 + 2O_2 \rightarrow (Ni_{0.5}Mn_{0.5})_2O_3 + 2CO_2$$
$$Li_2CO_3 \rightarrow Li_2O + CO_2$$
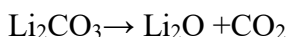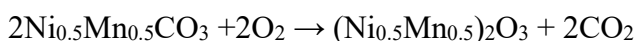
The microsphere morphology is retained after the annealing process and obtained $(Ni_{0.5}Mn_{0.5})_2O_3$ is highly porous owing to the release of CO_2 during thermal decomposition. And then, $19(Ni_{0.5}Mn_{0.5})_2O_3 + 31Li_2O + 6O_2 \rightarrow 50Li[Li_{0.24}Ni_{0.38}Mn_{0.38}]O_2$, and the fast outward diffusion of Mn, Ni, and Li atoms, and the slow inward diffusion of O atoms are proposed to be responsible for the formation of hollow cavities in the $Li[Li_{0.24}Ni_{0.38}Mn_{0.38}]O_2$ microspheres [41, 42].

CV was applied to investigate the redox reactions that occur during the cycling process (Figure

6). The CV curves of the hollow microspherical and nonspherical Li[Li$_{0.24}$Ni$_{0.38}$Mn$_{0.38}$]O$_2$ samples were recorded in the voltage range of 2.5–4.8 V at a scan rate of 0.2 mV s^{-1} for the initial cycle. The primary anodic peak at about 4.1 V is due to the oxidation of Ni^{2+}/Ni^{3+} to Ni^{4+} [43, 44].
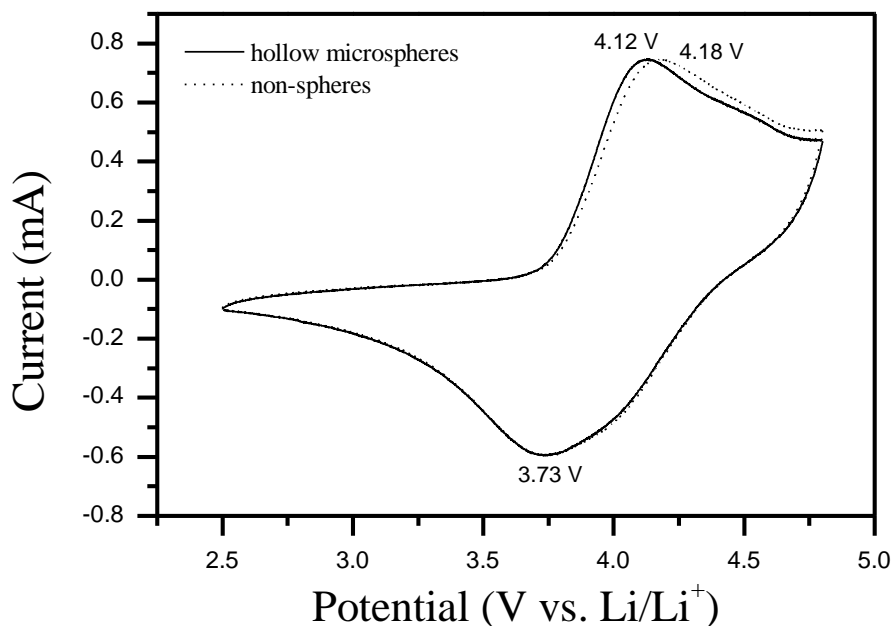

Figure 6. CV curves of the hollow microspherical and nonspherical Li[Li$_{0.24}$Ni$_{0.38}$Mn$_{0.38}$]O$_2$ (scan rate: 0.2 mV s^{-1}, potential range:2.5-4.8 V).

However, there is also a very small anodic peak located in the potential range of 4.5–4.8 V, which indicates that there is a very small amount of oxygen released from Li$_2$MnO$_3$-type component during the initial charge process for both the hollow microspherical and nonspherical Li[Li$_{0.24}$Ni$_{0.38}$Mn$_{0.38}$]O$_2$ materials [45]. In addition, the oxidation peaks of hollow microspherical and nonspherical Li[Li$_{0.24}$Ni$_{0.38}$Mn$_{0.38}$]O$_2$ are located at 4.12 and 4.18 V, respectively, whereas the reduction peaks are located at a similar voltage, 3.73 V. Therefore, the difference in the peak potentials of hollow microspherical Li[Li$_{0.24}$Ni$_{0.38}$Mn$_{0.38}$]O$_2$ is slightly smaller than that of nonspherical Li[Li$_{0.24}$Ni$_{0.38}$Mn$_{0.38}$]O$_2$, demonstrating the better reversibility of intercalation and deintercalation in hollow microspherical Li[Li$_{0.24}$Ni$_{0.38}$Mn$_{0.38}$]O$_2$.

The galvanostatic charge/discharge curves of the hollow microspherical and nonspherical Li[Li$_{0.24}$Ni$_{0.38}$Mn$_{0.38}$]O$_2$ samples at a current rate of 170 mA g^{-1} are presented in Figure 7a and 7b, it is evident that both the hollow microspherical and nonspherical materials exhibit a plateau at about 4.5 V in the initial charging curves, in agreement with the results of the CV experiments. This result can be mainly attributed to Li extraction accompanied by partial oxidation of the oxide ions, resulting in an irreversible loss of oxygen from the lattice [34, 46]. The characteristic reaction of Li-rich layered oxides during their initial charging process often leads to the formation of microcracks and amorphous domains on the surface, which in turn triggers a large irreversible capacity loss during the initial cycle that subsequently leads to capacity fading [47].
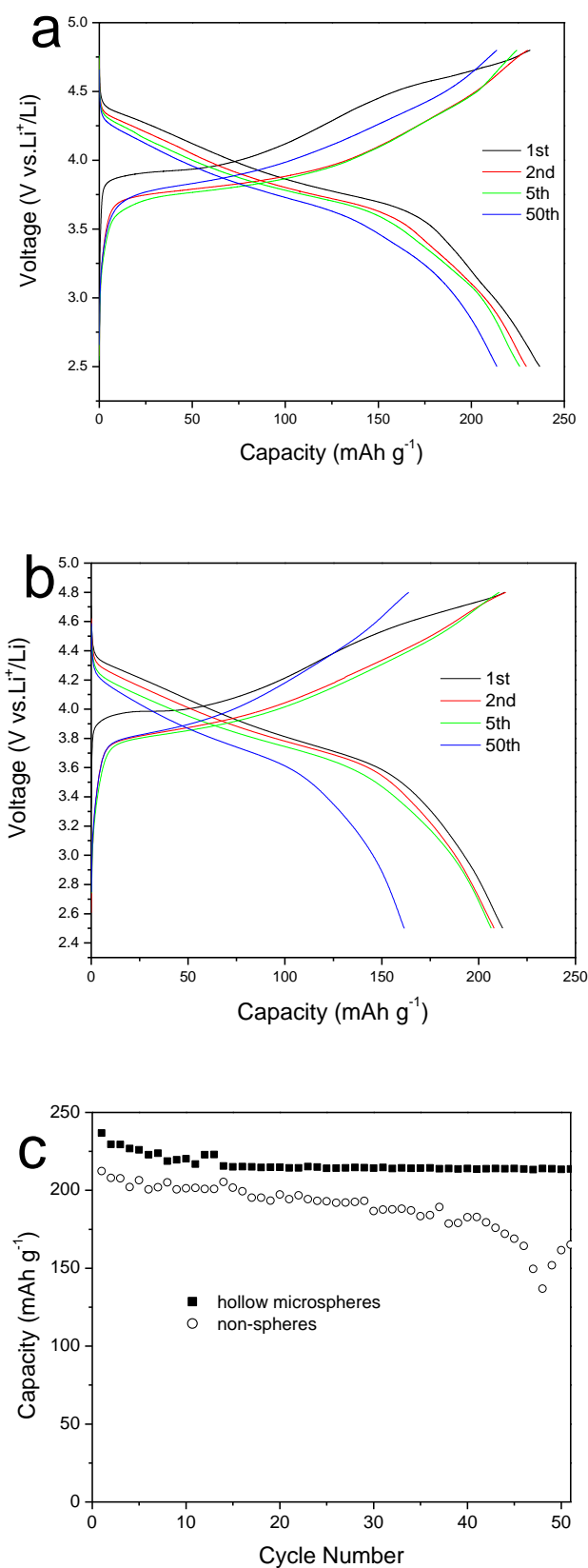
Figure 7. The initial charge and discharge curves of the hollow spherical (a) and nonspherical (b) Li[Li$_{0.24}$Ni$_{0.38}$Mn$_{0.38}$]O$_2$ samples in the voltage from 2.5 to 4.8 V at a rate of 170 mA g^{-1}, and charge and discharge capacity as a function of cycle number (c).

However, compared with Li-rich Li–Ni–Mn–Co–O and Li-Ni-Mn-O layered cathode materials [24, 48-53], the as-prepared Li-rich Li[$Li_{0.24}Ni_{0.38}Mn_{0.38}$]$O_2$ layered samples demonstrates only smaller initial charge and discharge capacities fading, indicating that the as-prepared Li[$Li_{0.24}Ni_{0.38}Mn_{0.38}$]$O_2$ layers inhibit electrochemical activation of Li_2MnO_4 in cathode material, which is accompanied by an extended release of oxygen and electrolyte side reaction during the initial charging process. However, no plateau is observed at about 4.5 V in the second and subsequent charging processes (Figure 7a), indicating that the release of oxygen and electrolyte side reactions only occurred during the first charging process. In addition, a discharge voltage lower than 3.5 V is not observed during the second and subsequent discharge processes, demonstrating that the Mn^{4+} are not reduced to a trivalent state by the irreversible release of oxygen during the first charging process [54]. Moreover, the cyclabilities of the hollow microspherical and nonspherical Li[$Li_{0.24}Ni_{0.38}Mn_{0.38}$]$O_2$ samples are ameliorated, as shown in Figure 7c. When charged and discharged over 2.5–4.8 V for 51 cycles, the nonspherical Li-rich material showed fast capacity fading, with only 77.83% of its initial capacity retained. In contrast, the hollow microspherical material showed a capacity of 213 mAh g^{-1}, with 90.2% of its initial capacity retained after 51 cycles. Thus, the electrochemical performance of the hollow microspherical Li[$Li_{0.24}Ni_{0.38}Mn_{0.38}$]$O_2$ is better than that of the nonspherical Li-rich material.
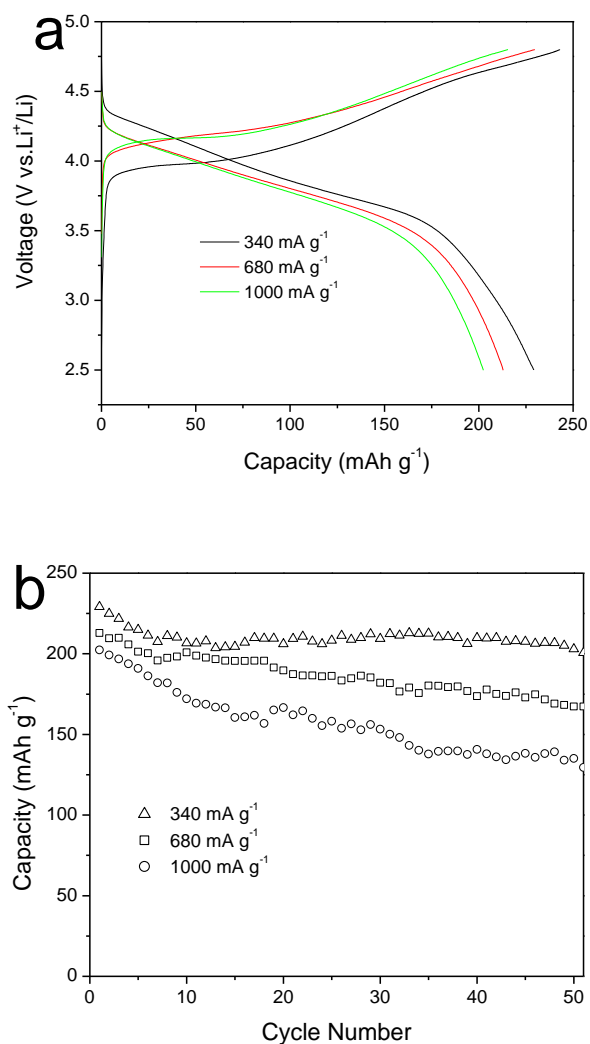
The initial capacity and current density of fabricated Li[$Li_{0.24}Ni_{0.38}Mn_{0.38}$]$O_2$ were compared with the Li-rich Li-Ni-Mn-O reported. The comparative results are provided in table 2.

Table 2. The iniatial capacity at the current density of the comparative Li-rich Li-Ni-Mn-O reported.

No.	Electrode material	Iniatial capacity(mAh g^{-1})	Current density(mA g^{-1})	Reference
1	$0.6Li_2MnO_3 \cdot 0.4LiMn_{1/3}Co_{1/3}Ni_{1/3}O_2$	276	30	55
2	$0.5Li_2MnO_3 \cdot 0.5LiNi_{0.8}Co_{0.1}Mn_{0.1}O_2$	262	12.5	56
3	$0.5Li(Ni_{0.375}Co_{0.25}Mn_{0.375})O_2 \cdot 0.5Li_2MnO_3$	252	21	57
4	$Li_{1.2}Ni_{0.13}Mn_{0.54}Co_{0.13}O_2$	269	25	58
5	$0.5Li_2MnO_3 \cdot 0.5LiNi_{0.5}Mn_{0.5}O_2$	242	20	59
6	$Li_{1.2}Ni_{0.2}Mn_{0.6}O_2$	250	12.5	60
7	$Li[Li_{0.2}Ni_{0.16}Mn_{0.56}Co_{0.08}]O_2$	284.5	44	61
8	$0.4Li_2MnO_3 \cdot 0.6LiNi_{1/3}Co_{1/3}Mn_{1/3}O_2$	269	20	62
9	$Li_{1.143}Mn_{0.544}Ni_{0.136}Co_{0.136}O_2$	287	unknown	63
10	$[Li_{0.2}Mn_{0.54}Ni_{0.13}Co_{0.13}]O_2$	343.2	25	64

Figure 8a displays the initial charge and discharge curves of hollow microspherical Li[$Li_{0.24}Ni_{0.38}Mn_{0.38}$]$O_2$ in the voltage range of 2.5–4.8 V at various current densities (340, 680 and 1000 mA g^{-1}). As shown, there is a decrease in the plateau at 4.5 V in the initial charging process as the current density increases. This observation does not mean that the amounts of released oxygen and electrolyte side reactions decrease during the initial charging process, but that the rates of oxygen release and Li extraction increase with increasing of current density. Therefore, these phenomena are indicated by the decrease in the plateau at 4.5 V in the initial charge curves. Further, the cycling performance of the hollow microspherical Li[$Li_{0.24}Ni_{0.38}Mn_{0.38}$]$O_2$ samples at various current densities

(340, 680 and 1000 mA g^{-1}) is shown in Figure 8b. The initial discharge capacities are 229, 213 and 202 mAh g^{-1}, respectively. After 51 cycles, the capacities decrease to 200, 167, and 129 mAh g^{-1}, corresponding to capacity retentions of 87.3%, 78.4% and 63.9%, respectively. Figure 8c shows that the storage capacity of the hollow microspheres is stable at each current density. It can be noticed that the specific capacity returns to its original value soon after the rate reverses back to 50 mA g^{-1}, revealing the superior reversibility of the hollow microspheres. Upon increasing the current density, the gradual reduction in the storage capacity of the hollow microspheres is not due to an irreversible structural change, but to diffusion-limited end-of-life polarization resulting from limited electronic conductivity and slow Li-ion diffusion, either across the electrolyte–electrode interface or within the bulk of the microspheres [15]. The remarkable electrochemical performance might be related to the advantageous structure of these hollow microspheres. Firstly, the hollow microspherical porous framework composed of nanoparticles with a large surface area affords a reduced Li-ion diffusion length, resulting in improved electrochemical kinetics. Secondly, the void space in the interior together with the porous shell provides abundant and hierarchical channels for facile penetration of the electrolyte into the active material.
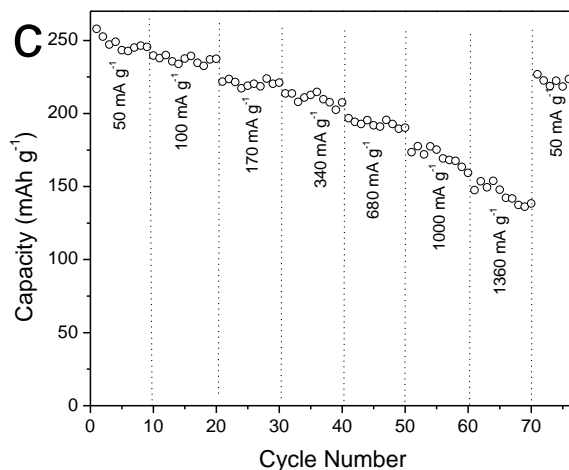
Figure 8. (a) The initial charge and discharge curves, (b) cycling performances and (c) discharge capacity of the hollow microspherical Li[Li$_{0.24}$Ni$_{0.38}$Mn$_{0.38}$]O$_2$ in the voltage from 2.5 to 4.8 V at different current density.

Thirdly, hollow microspherical Li[Li$_{0.24}$Ni$_{0.38}$Mn$_{0.38}$]O$_2$ could provide significantly improved structural integrity by partly mitigating the mechanical strain of the volume changes associated with repeated Li-ion intercalation/deintercalation processes during cycling, which might contribute greatly to the excellent cycling stability [31, 65].

4. CONCLUSIONS

In conclusion, Li-rich hollow microspherical Li[Li$_{0.24}$Ni$_{0.38}$Mn$_{0.38}$]O$_2$ as cathode material for Li-ion batteries was prepared by a coprecipitation approach followed by high-temperature calcination. Characterization revealed that the sample possesses a typical a-NaFeO$_2$ layered structure with a weak reflection corresponding to LiMnO$_6$, a low degree of cation mixing, and hollow microspheres with porous surfaces. Hollow microspherical Li[Li$_{0.24}$Ni$_{0.38}$Mn$_{0.38}$]O$_2$ exhibited a high discharge capacity of 213 mAh g^{-1} after 51 cycles in the potential range of 2.5–4.8 V at a current of 170 mA g^{-1}, with oxygen release and electrolyte side reactions only occurring in the first charging process. Further, as hollow microspherical Li[Li$_{0.24}$Ni$_{0.38}$Mn$_{0.38}$]O$_2$ delivered good cycling stability and rate capability, it is a promising cathode candidate for high-energy-density Li-ion batteries.

References

1. K. Bourzac, *Nature*, 526 (2015) S105.

2. H. Tavassol, E. M. C. Jones, N. R. Sottos, A. A. Gewirth, *Nature Mater.*, 15 (2016) 1182–1187.
3. Y. K. Sun, S. T. Myung, B. C. Park, J. Prakash, I. Belharouak, K. Amine, *Nature Mater.*, 8 (2009) 320 - 324.
4. T. Cao, C. Shi, N. Zhao, C. He, J. Li, E. Liu, *J. Phys. Chem. C*, 119 (2015) 28749−28756.
5. P. Oh, S. Myeong, W. Cho, M. J. Lee, M. Ko, H. Y. Jeong, J. Cho, *Nano. Lett.*, 14 (2014) 5965−5972.
6. C. H. Shen, L. Huang, Z. Lin, S. Y. Shen, Q. Wang, H. Su, F. Fu, X. M. Zheng, *ACS Appl. Mater. Interfaces*, 6 (2014) 13271−13279.
7. R. Benedek, H. Iddir, *J. Phys. Chem. C*, 121 (2017) 6492−6499.
8. H. Chen, M. S. Islam, *Chem. Mater.*, 28 (2016) 6656−6663.
9. B. Yue, X. Wang, J. Wang, J. Yao, X. Zhao, H. Zhang, W. Yu, G. Liu, X. Dong, *RSC Adv.*, 8 (2018) 4112–4118.
10. T. Tang, H. L. Zhang, *Electrochim. Acta*, 191 (2016) 263-269.
11. T. Zhao, N. Zhou, X. Zhang, Q. Xue, Y. Wang, M. Yang, L. Li, R. Chen, *ACS Omega*, 2 (2017) 5601−5610.
12. J. H. Song, A. Kapylou, H. S. Choi, B. Y. Yu, E. Matulevich, S. H. Kang, *J. Power Sources*, 313 (2016) 65-72.
13. J. Huang, H. Liu, T. Hu, Y. S. Meng, J. Luo, *J. Power Sources*, 375 (2018) 21-28.
14. Y. Zhao, M. Xia, X. Hu, Z. Zhao, Y. Wang, Z. Lv, *Electrochim. Acta*, 174 (2015) 1167-1174.
15. G. Kobayashi, Y. Irii, F. Matsumoto, A. Ito, Y. Ohsawa, S. Yamamoto, Y. Cui, J. Y. Son, Y. Sato, *J. Power Sources*, 303 (2016) 250-256.
16. F. Wu, X. Zhang, T. Zhao, L. Li, M. Xie, R. Chen, *ACS Appl. Mater. Interfaces*, 7 (2015) 3773−3781.
17. D. Chen, W. Tu, M. Chen, P. Hong, X. Zhong, Y. Zhu, Q. Yu, W. Li, *Electrochim. Acta*, 193 (2016) 45-53.
18. F. Zheng, C. Yang, X. Xiong, J. Xiong, R. Hu, Y. Chen, M. Liu, *Angew. Chem.-Int. Edit.*, 54 (2015) 13058–13062.
19. F. Wu, J. Liu, L Li, X. Zhang, R. Luo, Y. Ye, R. Chen, *ACS Appl. Mater. Interfaces*, 8 (2016) 23095−23104.
20. K. Jarvis, C. C. Wang, M. Varela, R. R. Unocic, A. Manthiram, P. J. Ferreira, *Chem. Mater.*, 29 (2017) 7668−7674.
21. D. Dai, B. Li, H. Tang, K. Chang, K. Jiang, Z. Chang, X. Yuan, *J. Power Sources*, 307 (2016) 665-672.
22. L. Yi, Z. Liu, R. Yu, C. Zhao, H. Peng, M. Liu, B. Wu, M. Chen, X. Wang, *ACS Sustainable Chem. Eng.*, 5 (2017) 11005−11015.
23. D.Luo , G. Li, C. Fu, J. Zheng, J. Fan, Q. Li, L. Li, *Adv. Energy Mater.*, 4 (2014) 1400062.
24. V. Pimenta, M. Sathiya, D. Batuk, A. M. Abakumov, D. Giaume, S. Cassaignon, D. Larcher, J. M. Tarascon, *Chem. Mater.*, 29 (2017) 9923−9936.
25. M. Wang, M. Luo, Y. Chen, L. Chen, S. Yan, Y. Ren, M. Chu, *J. Alloy Compd.*, 696 (2017) 891-899.
26. Y. P. Deng, Z. W. Yin, Z. G. Wu, S. J. Zhang, F. Fu, T. Zhang, J. T. Li, L. Huang, S. G. Sun, *ACS Appl. Mater. Interfaces*, 9 (2017) 21065−21070.
27. B. Qiu, C. Yin, Y. Xia, Z. Liu, *ACS Appl. Mater. Interfaces*, 9 (2017) 3661−3666.
28. M. Xu, L. Fei, W. Zhang, T. Li, W. Lu, N. Zhang, Y. Lai, Z. Zhang, J. Fang, K. Zhang, J. Li, H. Huang, *Nano. Lett.*, 17 (2017) 1670−1677.
29. A. Ito, D. Li, Y. Sato, M. Arao, M. Watanabe, M. Hatano, H. Horie, Y. Ohsawa, *J. Power Sources*, 195 (2010) 567-573.
30. Y. Qian, Y. Deng, Z. Shi, Y. Zhou, Q. Zhuang, G. Chen, *Electrochem. Commun.*, 27 (2013) 92-95.
31. Y. Yao, H. Liu, G. Li, H. Peng, K. Chen, *Mater. Chem. Phys.*, 143 (2014) 867-872.
32. M. M. Thackeray, S. H. Kang, C. S. Johnson, J. T. Vaughey, R. Benedek, S. A. Hackney, *J. Mater.*

Chem., 17 (2007) 3112–3125.

33. Z. H. Lu, D. D. MacNeil, J. R. Dahn, *Electrochem. Solid State Lett.*, 4 (2001) A191–A194.
34. A. R. Armstrong, M. Holzapfel, P. Novak, C. S. Johnson, S. H. Kang, M. M. Thackeray, P. G. Bruce, *J. Am. Chem. Soc.*, 128 (2006) 8694–8698.
35. S. J. R. Prabakar, S. C. Han, S. P. Singh, D. K. Lee, K. S. Sohn, M. Pyo, *J. Power Sources*, 209 (2012) 57-64.
36. C. Yu, G. S. Li, X. F. Guan, J. Zheng, L. P. Li, T. W. Chen, *Electrochim. Acta*, 81 (2012) 283-291.
37. M. Oishi, T. Fujimoto, Y. Takanashi, Y. Orikasa, A. Kawamura, T. Ina, H. Yamashige, D. Takamatsu, K. Sato, H. Murayama, H. Tanida, H. Arai, H. Ishii, C. Yogi, I. Watanabe, T. Ohta, A. Mineshige, Y. Uchimoto, Z. Ogumi, *J. Power Sources*, 222 (2013) 45-51.
38. K. Amine, H. Tukamoto, H. Yasuda, Y. Fujita, *J. Electrochem. Soc.*, 143 (1996) 1607-1613.
39. C. Lu, S. Yang, H. Wu, Y. Zhang, X. Yang, T. Liang, *Electrochim. Acta*, 209 (2016) 448-455.
40. T. Yang, N. Zhang, Y. Lang, K. Sun, *Electochim. Acta*, 56 (2011) 4058-4064.
41. L. Zhou, D. Zhao, X. W. Lou, *Angew. Chem. Int. Ed.*, 51 (2012) 239 –241.
42. X. W. Lou, L. A. Archer, Z. C. Yang, *Adv. Mater.*, 20 (2008) 3987 –4019.
43. H. Yu, H. Kim, Y. Wang, P. He, D. Asakura, Y. Nakamura, H. Zhou, *Phys. Chem. Chem. Phys.*, 14 (2012) 6584-6595.
44. B. Song, M. O. Lai, L. Lu, *Electrochim. Acta*, 80 (2012) 187-195.
45. H. Liu, C. Du, G. Yin, B. Song, P. Zuo, X. Cheng, Y. Ma, Y. Gao, *J. Mater. Chem. A*, 2 (2014) 15640-15646.
46. Z. Lu, J. R. Dahn, *J. Electrochem. Soc.*, 149 (2002) A815-A822.
47. Z. Lu, J. R. Dahn, *J. Electrochem. Soc.*, 149 (2002) A1454-A1459.
48. X. Yu, Y. Ly, L. Gu, H. Wu, S. M. Bak, Y. Zhou, K. Amine, S. N. Ehrlich, H. Li, K. W. Nam, X. Q. Yang, *Adv. Energy Mater.*, 4 (2014) 1300950.
49. P. K. Nayak, J. Grinblat, M. Levi, E. Levi, S. Kim, J. W. Choi, D. Aurbach, *Adv. Energy Mater.*, 6 (2016) 1502398.
50. Z. Wei, W. Zhang, F. Wang, Q. Zhang, B. Qiu, S. Han, Y. Xia, Y. Zhu, Z. Liu, *Chem. Eur. J.*, 21 (2015) 7503 –7510.
51. E. McCalla, A. W. Rowe, J. Camardese, J. R. Dahn, *Chem. Mater.*, 25 (2013) 2716−2721.
52. J. Lin, D. Mu, Y. Jin, B. Wu, Y. Ma, F. Wu, *J. Power Sources*, 230 (2013) 76-80.
53. P. K. Nayak, J. Grinblat, E. Levi, B. Markovsky, D. Aurbach, *J. Power Sources*, 318 (2016) 9-17.
54. D. Liu, J. Han, J. B. Goodenough, *J. Power Sources*, 195 (2010) 2918-2923.
55. G. Liu, S. Li, J. Mei, L.-M. Liu, Y. Cui, H. Liu, *J. Power Sources*, 353 (2017) 51-57.
56. J.-L. Shi, D.-D. Xiao, M. Ge, X. Yu, Y. Chu, X. Huang, X.-D. Zhang, Y.-X. Yin, X.-Q. Yang, Y.-G. Guo, L. Gu, L.-J. Wan, *Adv. Mater.*, 30 (2018) 1705575 (1-8).
57. X. Yu, Y. Lyu, L. Gu, H. Wu, S.-M. Bak, Y. Zhou, K.l Amine, S. N. Ehrlich, H. Li, K.-W. Nam, X.-Q. Yang, *Adv. Energy Mater.*, (2013) 1-11, DOI: 10.1002/aenm.201300950.
58. V. Pimenta, M. Sathiya, D. Batuk, A. M. Abakumov, D. Giaume, S. Cassaignon, D. Larcher, J.-M. Tarascon, *Chem. Mater.*, 29 (2017) 9923−9936.
59. P. Oh, S. Myeong, W. Cho, M.-J. Lee, M. Ko, H. Y. Jeong, J. Cho, *Nano Lett.*, 14 (2014) 5965−5972
60. M. Zhang, H. Liu, Z. Liu, C. Fang, Y. S. Meng, *ACS Appl. Energy Mater.*, unpublished, DOI: 10.1021/acsaem.8b00545.
61. H. Lee, S. B. Lim, J. Y. Kim, M. Jeong, Y. J. Park, W.-S. Yoon, *ACS Appl. Mater. Interfaces*, 10 (2018) 10804−10818.
62. L. Yi, Z. Liu, R. Yu, C. Zhao, H. Peng, M. Liu, B Wu, M. Chen, X. Wang, *ACS Sustainable Chem. Eng.*, 5 (2017) 11005−11015.
63. H. Guoa, Z. Wei, K. Jia, B. Qiu, C. Yin, F. Meng, Q. Zhang, L. Gu, S. Han, Y. Liu, H. Zhao, W. Jiang, H. Cui, Y. Xia, Z. Liu, *Energy Storage Mater.*, 16 (2019) 220‐227.
64. J. Zhao, X. Kuai, X. Dong, H. Wang, W. Zhao,L. Gao, Y. Wang, R. Huang, *J. Alloy. Compd.*, 732

(2018) 385-395.
65. G. Zhang, L. Yu, H. B. Wu, H. E. Hoster, X. W. Lou, *Adv. Mater.*, 24 (2012) 4609-4613.